

# High-pressure phase transition, pore collapse and amorphisation in the siliceous 1D zeolite, TON.

*Jean-Marc Thibaud<sup>†</sup>, Jérôme Rouquette<sup>†</sup>, Patrick Hermet<sup>†</sup>, Kamil Dziubek<sup>§,||</sup>, Federico A. Gorelli<sup>§,‡</sup>, Mario Santoro<sup>§,‡</sup>, Gaston Garbarino<sup>⊥</sup>, Frederico G. Alabarse<sup>∇</sup>, Olivier Cambon<sup>†</sup>, Francesco Di Renzo<sup>†</sup>, Arie van der Lee<sup>#</sup>, Julien Haines<sup>\*†</sup>*

<sup>†</sup>Institut Charles Gerhardt Montpellier, UMR 5253 CNRS-Université de Montpellier-ENSCM, 34095 Montpellier Cedex 5, France.

<sup>§</sup>European Laboratory for Non Linear Spectroscopy (LENS), 50019 Sesto Fiorentino, Italy.

<sup>||</sup>Faculty of Chemistry, Adam Mickiewicz University, Umultowska 89b, 61-614 Poznań, Poland.

<sup>‡</sup>Istituto Nazionale di Ottica, CNR-INO, 50019 Sesto Fiorentino, Italy.

<sup>⊥</sup>ESRF, 71, avenue des Martyrs, 38000 Grenoble, France.

<sup>∇</sup>Synchrotron Soleil, L'Orme les Merisiers, Saint Aubin – BP48, 91192 Gif sur Yvette, France.

<sup>#</sup>Institut Européen des Membranes de Montpellier, UMR CNRS 5635, Université de Montpellier, 34095 Montpellier Cedex 5, France

KEYWORDS: Zeolite, Phase transition, High-pressure, Infrared spectroscopy, X-ray diffraction.

ABSTRACT. The siliceous zeolite TON with a 1-D pore system was studied at high pressure by x-ray diffraction, infrared spectroscopy and DFT calculations. The intrinsic behavior of this material was investigated using non-penetrating pressure transmitting media. Under these conditions, a phase transition from the  $Cmc2_1$  to a  $Pbn2_1$  structure occurs at 0.7 GPa with cell doubling based on Rietveld refinements. The pores begin to collapse with a strong increase in their ellipticity. Upon decreasing the pressure below this value the initial structure was not recovered. This is in good agreement with DFT calculations, which indicate that the  $Cmc2_1$  phase is dynamically unstable on the absence of guests in the pores. Irreversible, progressive pressure induced amorphisation occurs upon further increases in pressure up to 20 GPa. These changes are confirmed in the mid- and far-infrared spectra by peak splitting at the  $Cmc2_1$  to  $Pbn2_1$  phase transition and strong peak broadening at high pressure due to amorphisation.

## 1. Introduction

Zeolites are porous aluminosilicates built up of corner-sharing  $TO_4$  ( $T = \text{Si, Al}\dots$ ) tetrahedra with many applications in catalysis, separation, ion exchange among others. Due to their high porosity, zeolites undergo very important changes as a function of pressure. There are several examples of phase transitions<sup>1-5</sup>, involving tilting of the constituent tetrahedral and/or changes in the ring structures. Pressure also can induce pore collapse and transformation to an amorphous state<sup>2, 5-20</sup>. This amorphous form can retain topological order from the parent crystalline phase and is distinct from normal glass<sup>13, 15-16, 18-19</sup>.

Siliceous zeolites also have many important applications in adsorption, catalysis, gas separation and storage and can also be considered as model materials as they contain essentially only  $\text{SiO}_4$  tetrahedra. A large number of studies have been performed on the MFI (Mobil-five) system, silicalite-1 at high pressure<sup>21</sup>, which has a 3D interconnected pore system. This material undergoes a monoclinic to orthorhombic phase transition under pressure<sup>2</sup> followed by pore collapse and complete irreversible amorphisation<sup>18</sup>. A simpler zeolite TON (theta-1) with a 1D pore system<sup>22</sup> is also of interest for catalysis and as hydrophobic host materials in molecular spring systems<sup>23</sup> and insulating host systems in conducting polymer/zeolite nanocomposites<sup>24</sup>. TON has an orthorhombic structure, space group  $Cmc2_1$  with 1D pores in the  $c$  direction<sup>22, 25-26</sup>. The framework is built up of 5, 6 and 10 membered rings of  $\text{SiO}_4$  tetrahedra. The pores are elliptical with free diameters of  $4.6 \times 5.7 \text{ \AA}$ . The goal of the present study is to investigate high pressure structural changes and phase stability of the siliceous zeolite TON.

## 2. Experimental and theoretical methods

**A. Synthesis and calcination of the TON zeolite.** The TON zeolite was prepared by sol-gel techniques using triethylenetetramine as the structure directing agent followed by crystallization at 170°C under hydrothermal conditions as described previously<sup>27</sup>. The sample was calcined in air at 550°C to remove the organic template. The sample was characterized by infrared spectroscopy, x-ray diffraction, thermal gravimetric analysis and nitrogen adsorption isotherms. The sample corresponded to pure TON with a trace of residue from the template.

**B. High-pressure, x-ray diffraction powder experiments on the TON zeolite.** Angle-dispersive, high-pressure x-ray diffraction was performed on the ID09A beamline at the ESRF synchrotron. The incident wavelength was 0.414132 Å and the distance from the sample to the MAR555 Flatpanel detector was 399.7462 mm. Acquisition was performed over a 6° range in  $\omega$ . TON powder along with a ruby sphere was placed along with a ruby in the 110  $\mu\text{m}$  diameter hole of a stainless steel gasket preindented to 50  $\mu\text{m}$  fixed to one anvil of a membrane DAC equipped with Boehler–Almax diamonds. DAPHNE7474<sup>28</sup> was added as a pressure-transmitting medium. Ruby was used as a pressure calibrant and the pressure was determined based on the shift of ruby R<sub>1</sub> fluorescence line<sup>29</sup>. Integration of the images was performed using FIT2D<sup>30</sup>. Both full-profile fitting to obtain the unit cell parameters and Rietveld refinements were performed using the program Fullprof<sup>31</sup>. Soft constraints were applied to the Si-O distances, O-O distances and/or the O-Si-O angles. Crystal structure were plotted using the program VESTA<sup>32</sup>. Bulk moduli were obtained by fitting P-V data using the program EoSFit7c<sup>33</sup>.

**C. High-pressure infrared spectroscopy experiments on the TON zeolite.** Mid- and far-Infrared (IR) spectra under high pressure were obtained using synchrotron radiation at the Advanced Infrared Line Exploited for Spectroscopy beamline (AILES, Synchrotron SOLEIL) equipped with a Bruker instruments IFS 125 Fourier transform infrared (FT-IR) spectrometer modified to operate with the synchrotron source<sup>34</sup>. Mid-IR spectra (4000-400  $\text{cm}^{-1}$ ) were obtained up to 6 GPa using a MCT (5000-600  $\text{cm}^{-1}$ ) detector and a KBr beamsplitter. The Far-IR spectra were obtained up to 10 GPa using a 6  $\mu\text{m}$  Mylar beamsplitter and a 4.2 K Si-bolometer detector (700-10  $\text{cm}^{-1}$ ). The spectra were measured with a resolution of 2  $\text{cm}^{-1}$  with 400 and 800 scans in the far- and mid-IR, respectively. Additional high pressure mid-infrared measurements up to 15 GPa (1  $\text{cm}^{-1}$  resolution) were performed in the laboratory using a Bruker IFS-120 HR Fourier transform infrared spectrometer, equipped with an optical beam condenser based on ellipsoidal mirrors. A KBr beamsplitter and an MCT detector were used.

The gasket thickness was 50-60  $\mu\text{m}$  with a hole diameter of 250  $\mu\text{m}$ . This limited the far-IR range to 50  $\text{cm}^{-1}$  in the diamond anvil cell (DAC). The sample was mixed with was KBr for the mid-IR and polyethylene (PE) for the far-IR as a pressure-transmitting medium, and loaded in the DAC inside a glovebox ( $p_{\text{H}_2\text{O}} < 4$  ppm). The KBr was dehydrated at 120  $^{\circ}\text{C}$  under  $10^{-6}$  mbar and PE at ambient temperature under  $10^{-6}$  mbar and both were transferred to the glovebox. Pressure was also measured using the ruby fluorescence method<sup>29</sup>.

**C. Density functional theory calculations (DFT) on the TON zeolite.** DFT based calculations were performed with the SIESTA package<sup>35</sup> and the generalized gradient approximation to the exchange correlation functional as proposed by Perdew, Burke and Ernzerhof<sup>36</sup>. Core electrons are replaced by nonlocal norm-conserving pseudopotentials. The

valence electrons are described by a double- $\zeta$  singly polarized basis set. The localization of the basis was controlled by an energy shift of 50 meV. Real space integration was performed on a regular grid corresponding to a plane-wave cutoff of 350 Ry. Van der Waals corrections (DFT-D) were considered using the semi-empirical dispersion potential parametrized by Grimme<sup>37</sup>.

Three space groups were considered:  $Cmc2_1$ ,  $Pbn2_1$  and  $P2_1$ . Atomic positions were relaxed using a conjugate gradient until the maximum residual atomic force was smaller than 0.01 eV/Å. Lattice parameters were fixed at 2 GPa for the  $Pbn2_1$  and  $P2_1$  structures whereas no condition on the pressure was given for the  $Cmc2_1$  structure. Structural relaxation was performed using a  $8 \times 8 \times 8$ ,  $6 \times 6 \times 8$  and  $6 \times 8 \times 6$   $k$ -point mesh for the  $Cmc2_1$ ,  $Pbn2_1$  and  $P2_1$  structures, respectively.

The infrared spectra were calculated according to Ref<sup>38</sup>. In this context, zone-center phonons were calculated within the harmonic approximation by finite difference of the Hellmann–Feynman forces with an atomic displacement of 0.03 Å and using the same  $k$ -point mesh considered for the relaxations. Born effective charges are computed using the Berry phase technique<sup>39</sup>. Positive and negative displacements are used to minimize the anharmonic effects both for the calculation of the Born effective charges and the zone-center phonons.

### 3. Results and discussion

**A. X-ray powder diffraction of TON in a non-penetrating pressure medium.** The initial structure of TON could be refined using the structural model from the single crystal structure determination of Marler<sup>25</sup> in the orthorhombic  $Cmc2_1$  space group (Figure 1 and Tables 1 and 2). In order to have a good fit and a stable refinement, it was necessary to include a small amount of atoms in the pores. This could correspond to the residue from the structure directing agent or

adsorbed species and were modelled by carbon atoms with partial occupancy. Due to the large number of atoms in the framework, it was necessary to include soft constraints on the distances and angles in the SiO<sub>4</sub> tetrahedra.

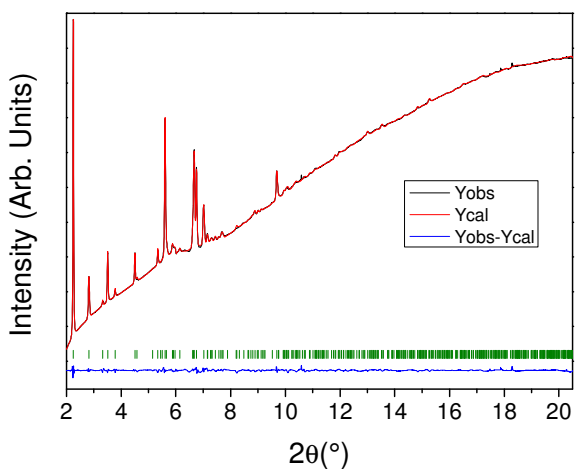
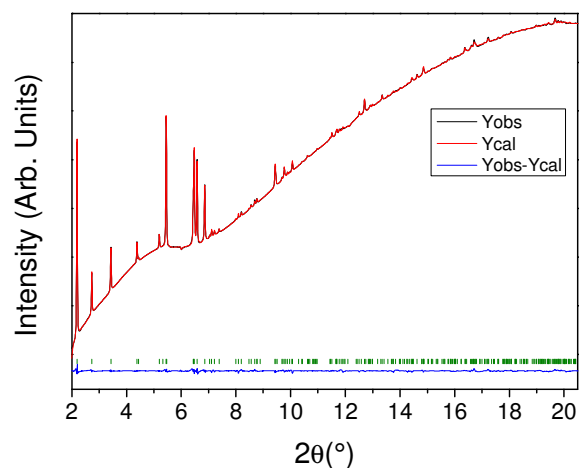


**Figure 1.** Experimental (black), calculated (red) and difference (blue) profiles obtained from the Rietveld refinement of the *Cmc*2<sub>1</sub> structure of TON at ambient pressure (top) and the *Pbn*2<sub>1</sub> structure at 1.7 GPa (bottom). Vertical bars indicate the calculated positions of the Bragg reflections.

At close to 0.7 GPa new diffraction peaks were observed (Figure 2), which could be indexed as  $hkl$ ,  $h+k \neq 2n$ , indicating the loss of  $C$  centering. The peaks were also slightly broadened, indicating a degree of strain. The change in reflection conditions is consistent with a doubling of the primitive unit with group-subgroup transition from  $Cmc2_1$  to  $Pmc2_1$ ,  $Pbn2_1$ ,  $Pbc2_1$  or  $Pmn2_1$  space groups. Very weak peaks were observed which violated the reflection conditions for all the possible glide planes and thus a structural model with monoclinic  $P2_1$  space group was considered. The structure could then be readily refined. The observed structural changes involve each second layer of pores becoming inequivalent and compressing along opposite diagonals of the pores. This process is reminiscent of the mechanism of pore collapse in zeolite RHO as a function of degree of hydration and temperature<sup>40</sup>. There are also distortions to all the rings of tetrahedra in the  $\text{SiO}_2$  framework involving changes to the intertetrahedral bridging angles. The monoclinic angle refined to  $90^\circ$  and close inspection of the structure indicated that the overall topology is possibly only slightly distorted from an orthorhombic system with  $b$  and  $n$  glide planes. The main difference is that in the monoclinic space group the pores in each second layer have different diameters; however, the Bragg R-factor was equivalent in orthorhombic and monoclinic symmetry in spite of relatively important differences in atomic positions around the second layer of pores. No significant difference between the two models was observed for the very weak peaks that violated the reflection conditions for the glide planes. The orthorhombic model with many fewer structural parameters was thus used for the refinements (Figures 1 and 3 and Tables 1 and 3), although a very slight monoclinic distortion is possible. The additional  $hkl$ ,  $h+k \neq 2n$  reflections become more intense as function of pressure (Figure 2) due to the increase in the distortion (flattening) of the pores (Figure 4). This distortion is progressive from the transition pressure of 0.7 GPa up to 1.7 GPa on compression.



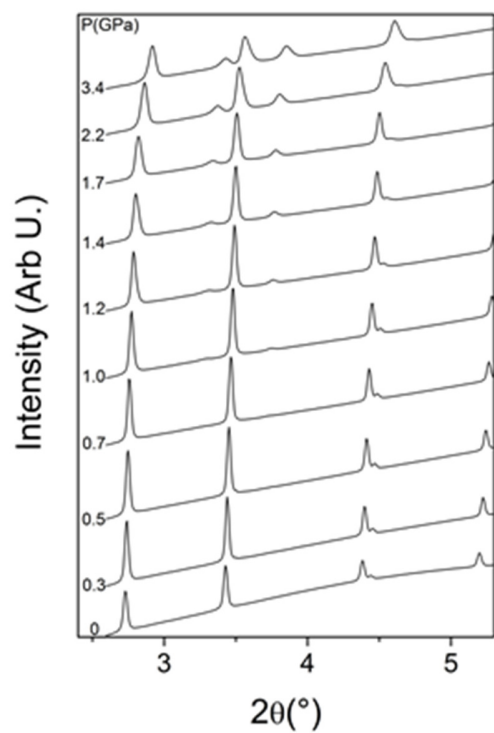
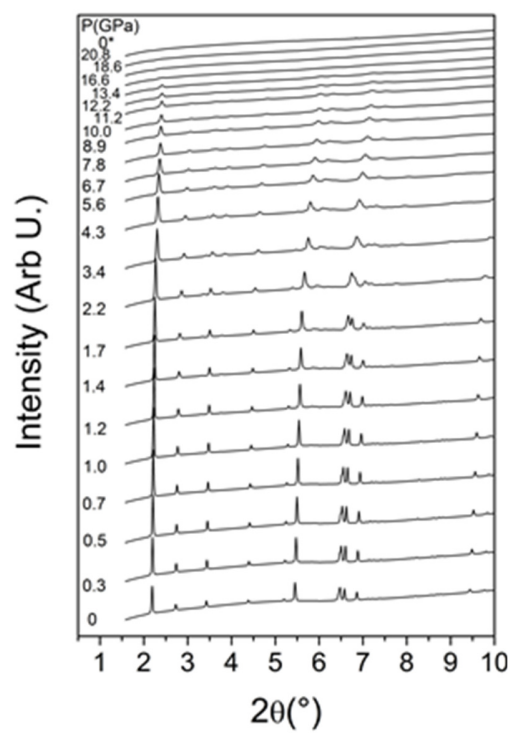


**Figure 2.** X-ray diffraction patterns of TON (top) as a function of pressure ( $\lambda=0.414132 \text{ \AA}$ ). A zoom of the low pressure data is shown below (bottom). \* = data obtained on pressure release.

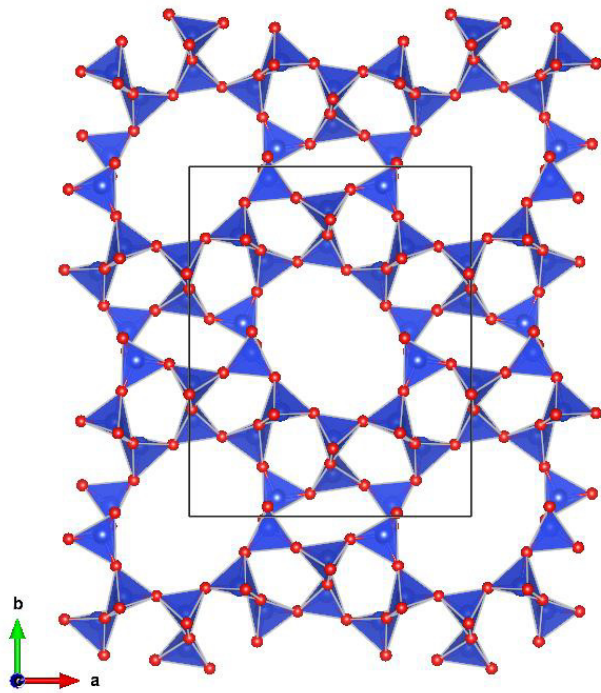
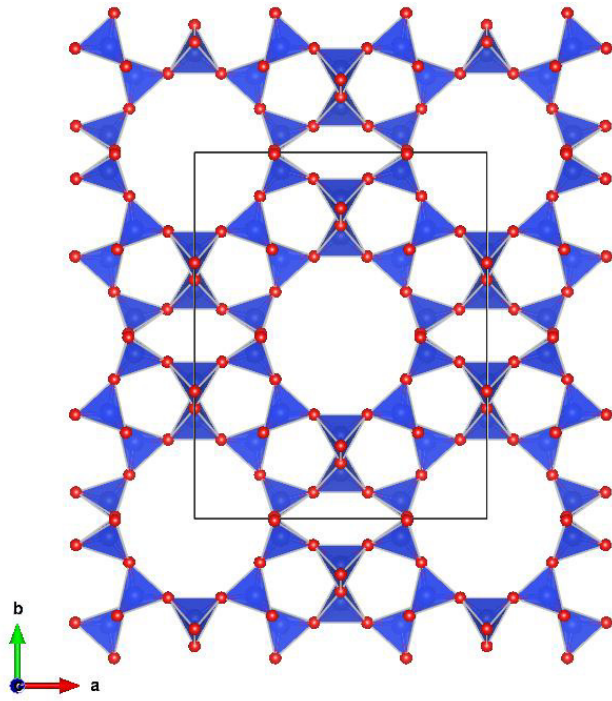


**Figure 3.** Polyhedral representation of the  $Cmc2_1$  structure of TON at ambient pressure (top) and the  $Pbn2_1$  structure at 1.7 GPa (bottom). Blue and red spheres represent the silicon and oxygen atoms, respectively.

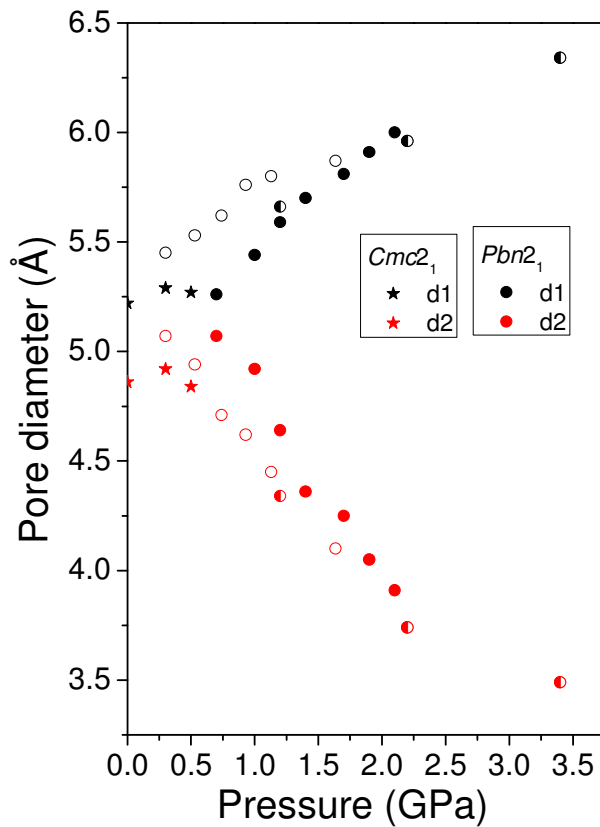


**Figure 4.** Pore diameters as a function of pressure. Solid symbols correspond to the points obtained on compression. Open symbols correspond to points obtained during the decompression pressure cycle between 2.1 and 0.3 GPa. Half-solid symbols represent the data obtained for the high pressure phase on compression after pressure cycling.

**Table 1.** Lattice parameters of TON at ambient pressure (orthorhombic, space group  $Cmc2_1$ ) and at 1.7 GPa (orthorhombic, space group  $Pbn2_1$ ) and profile  $R_p$ , weighted profile  $R_{wp}$  and Bragg  $R_{Bragg}$  agreement factors<sup>41-42</sup>.


	P = 0.1 MPa	P= 1.7 GPa
$a$ (Å)	13.8436(3)	13.5365(3)
$b$ (Å)	17.3834(7)	16.8149(6)
$c$ (Å)	5.0364(1)	4.9029(1)
$V$ (Å <sup>3</sup> )	1212.02(6)	1115.98(5)
$R_p$ (%)	12.0	12.2
$R_{wp}$ (%)	4.3	4.6
$R_{Bragg}$ (%)	5.0	6.0

**Table 2.** Atomic positions, atomic displacement parameters and occupation factors of TON at ambient pressure (orthorhombic, space group  $Cmc2_1$ ). The carbon atoms account for the residue in the pores (decomposition products of the organic template, adsorbed species etc.).

$Cmc2_1$	x	y	Z	$B_{iso}$ ( $\text{\AA}^2$ )	Occ.
O1	0.093(2)	0.427(2)	0.70(2)	2.7(7)	1.0
O2	0.091(2)	0.215(3)	0.22(2)	2.7(7)	1.0
O3	0.276(3)	0.380(2)	0.69(2)	2.7(7)	1.0
O4	0.226(3)	0.495(4)	-0.01(1)	2.7(7)	1.0
O5	0.265(4)	0.264(3)	0.380(8)	2.7(7)	1.0
O6	0	0.300(3)	0.560(8)	2.7(7)	1.0
O7	0	0.347(3)	0.068(7)	2.7(7)	1.0
Si1	0.294(2)	0.048(1)	0.225(6)	3.1(4)	1.0
Si2	0.206(1)	0.210(1)	0.180(6)	3.1(4)	1.0
Si3	0	0.273(2)	0.25	3.1(4)	1.0
Si4	0	0.372(2)	0.760(6)	3.1(4)	1.0
C1	0.5	0.445(5)	0.1171	0.8(9)	0.40(4)
C2	0.5	0.445(5)	0.3671	0.8(9)	0.40(4)

**Table 3.** Atomic positions, atomic displacement parameters and occupation factors of TON at 1.7 GPa (orthorhombic, space group  $Pbn2_1$ ). The carbon atoms account for the residue in the pores (decomposition products of the organic template, adsorbed species etc.).

<i>Pbn</i> 2 <sub>1</sub>	x	y	Z	B <sub>iso</sub> (Å <sup>2</sup> )	Occ.
O1	0.074(2)	0.566(2)	0.18(1)	2.7(6)	1.0
O1_2	0.612(2)	0.079(2)	0.21(1)	2.7(6)	1.0
O2	0.060(2)	0.797(2)	0.75(1)	2.7(6)	1.0
O2_2	0.617(2)	0.267(3)	0.69(1)	2.7(6)	1.0
O3	0.238(3)	0.644(2)	0.17(1)	2.7(6)	1.0
O3_2	0.798(3)	0.104(2)	0.18(1)	2.7(6)	1.0
O4	0.233(3)	0.493(2)	0.339(7)	2.7(6)	1.0
O4_2	0.727(3)	0.971(2)	0.356(7)	2.7(6)	1.0
O5	0.202(3)	0.793(2)	0.081(6)	2.7(6)	1.0
O5_2	0.751(3)	0.244(2)	0.066(6)	2.7(6)	1.0
O6	0.483(4)	0.805(2)	0.567(6)	2.7(6)	1.0
O7	0.503(4)	0.846(2)	0.046(6)	2.7(6)	1.0
S1	0.283(2)	0.967(2)	0.662(8)	4.5(4)	1.0
S1_2	0.807(2)	0.445(2)	0.690(9)	4.5(4)	1.0
S2	0.175(2)	0.802(2)	0.720(9)	4.5(4)	1.0
S2_2	0.734(2)	0.268(2)	0.746(9)	4.5(4)	1.0
S3	0.487(2)	0.777(2)	0.217(8)	4.5(4)	1.0
S4	0.492(2)	0.876(2)	0.75	4.5(4)	1.0
C1	0.050(4)	0.050(4)	0.1171	2(1)	0.204
C2	0.050(4)	0.050(4)	0.3671	2(1)	0.204
C3	-0.055(4)	-0.055(4)	0.1171	2(1)	0.204
C4	-0.055(4)	-0.055(4)	0.3671	2(1)	0.204

The sample was cycled from 2.1 GPa down to 0.3 GPa. The additional peaks remained at 0.3 GPa, indicating that the high pressure structure was retained with the pores remaining collapsed to a certain degree (Figure 4). This pressure cycling resulted in an increase in the width of the diffraction lines. Upon recompressing the sample, the intensity of the diffraction lines remained relatively stable up to 3.4 GPa, which is close to the hydrostatic limit for DAPHNE7474<sup>28</sup>. 

A loss of overall intensity is observed from 4 GPa up to 16.6 GPa (Figure 2), at which only a very weak remaining feature is observed close to the position at which the strongest diffraction line was observed at lower pressure. This feature strongly decreased in intensity at the maximum pressure reached of 20.8 GPa, with full disappearance of the diffraction lines on pressure release. This result is consistent with the formation of an amorphous material. This process has also been observed in a significant number of other zeolites<sup>2, 5-19</sup> and has been linked to geometrical distortions associated with pore collapse, while retaining the topology of the starting crystalline phase<sup>18-19</sup>.

Unit cell parameters (Figure 5) and volume (Figure 6) were obtained from the Rietveld refinements as a function of pressure up to 13.4 GPa. The low-pressure *Cmc2<sub>1</sub>* structure is 1.5 times more compressible along the pore axis (*c* direction) than in the *xy* plane. This relative stiffness in the *xy* plane is very clear from the plot of pore diameter as a function of pressure, which does not vary significantly for the *Cmc2<sub>1</sub>* structure. This higher compressibility along the pore direction is similar to other materials with 1D porosity<sup>5, 43</sup> due to the reduction in intertetrahedral bridging angles lying out of the *xy* plane and in the present case particularly those in the five-membered rings of tetrahedra. The phase transition can clearly be seen by strong decrease particularly in the *b* cell parameter (Figure 5) and in the relative volume (Figure 6) beginning near 0.7 GPa and becoming more and more marked as the pores collapse (Figure 4).

The overall compression is 13% along **b**, 8.5 % along **c** and 6.5% along **a** over the pressure range investigated. This is linked to the increase in ellipticity of the pores. In the low-pressure  $Cmc2_1$  structure the free diameters of the pores 5.22(9)Å and 4.86(6)Å are aligned respectively along the **b** and **a** directions. At the transition the structure distorts and the free diameters lie along the [110] et  $[\bar{1}10]$  directions, that is the larger free diameter is no longer along **b**, but strongly rotated in the  $xy$  plane, thereby decreasing the  $b/a$  cell parameter ratio. The distortion remains on decompression down to at least 0.3 GPa as can be seen from the pore diameters and particularly the cell parameter  $b$  for which the behavior is very different from the first set of data obtained on compression.



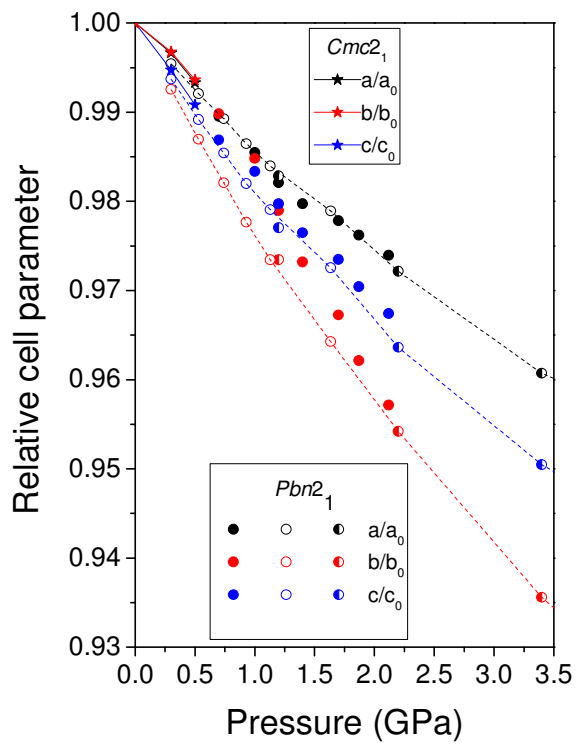
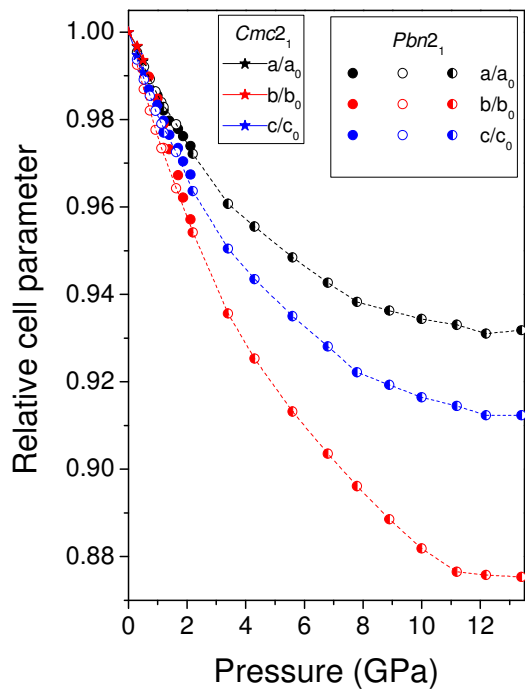


**Figure 5.** Relative lattice parameters of TON (top) as a function of pressure. A zoom of the low pressure data is shown below (bottom). Solid symbols correspond to the points obtained on compression. Open symbols correspond to points obtained during the decompression pressure cycle between 2.1 and 0.3 GPa. Half-solid symbols represent the data obtained for the high pressure phase on compression after pressure cycling. Dashed lines represent the behavior of the high pressure phase after pressure cycling.

A progressive decrease in cell volume is also observed beginning at the phase transition with respect to the extrapolated volume of the  $Cmc2_1$  phase. On decompression, the unit cell volume is lower due to a degree of irreversibility in the pore collapse. The  $Pbn2_1$  phase is denser with a relative volume, which at 0.3 GPa is 0.6% lower than that of the  $Cmc2_1$  phase at the same pressure. The  $Pbn2_1$  phase is also 40% more compressible than the  $Cmc2_1$  phase due to its lower symmetry and new compression mechanism involving increased pore ellipticity and subsequent collapse. This value is based on the bulk moduli calculated using a second-order Birch-Murnaghan equation of state<sup>44</sup> for the low-pressure phase ( $B_0 = 22$  (2) GPa) and a  $B_0$  of 15.8(4) GPa using the points below 4 GPa in the decompression-recompression pressure cycle for the high-pressure phase. These values are typical of those of siliceous zeolites, such as silicalite-1<sup>2</sup>. The overall volume decrease is 25% up to 13.5 GPa. Above 12 GPa, the volume appears to no longer decrease. Such non-equilibrium behavior is observed for many zeolites<sup>2, 13, 15-18</sup> during the amorphization process, which is likely to begin at pressures above 4 GPa based on the decrease in intensity of the diffraction lines. As the amorphous fraction strongly increases above 12 GPa, the sample exhibits a complex microstructure corresponding to crystallites in a denser

amorphous matrix. As zones become amorphous with an important volume change, local depressurization occurs.

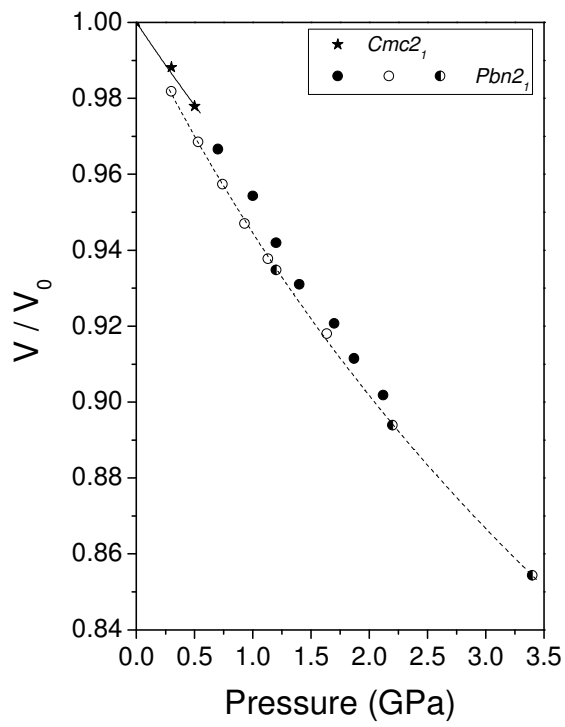
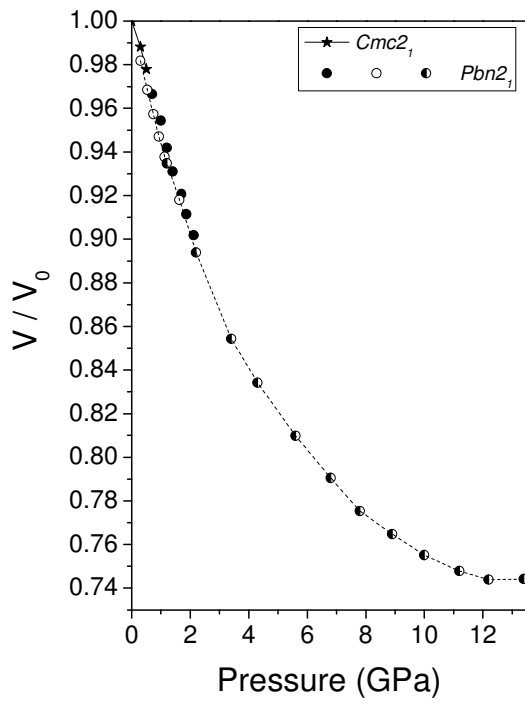


**Figure 6.** Relative volume of TON (top) as a function of pressure. A zoom of the low pressure data is shown below (bottom). Solid symbols correspond to the points obtained on compression. Open symbols correspond to points obtained during the decompression pressure cycle between 2.1 and 0.3 GPa. Half-solid symbols represent the data obtained for the high pressure phase on compression after pressure cycling. The dashed line represents the behavior of the high pressure phase after pressure cycling.

**B. Infrared spectroscopy at high pressure.** Group theory predicts that TON with the space group  $Cmc2_1$  will have  $29 A_1 + 25 A_2 + 25 B_1 + 29 B_2$  modes. Of these, 28  $A_1$ , 24  $B_1$  and 28  $B_2$  modes are active in the infrared. Infrared spectra in both the mid- and far-IR regions (Table 4, Figures 7-8) were in good agreement with previous work<sup>45-46</sup>. The results are also in good agreement with DFT calculations (Figure 9). Changes were observed beginning at 0.5 GPa (Figures 7 and 10), in particular a marked splitting of the secondary building unit ring mode near  $570 \text{ cm}^{-1}$  in the far-IR. Other modes were also observed to split such as bending modes below  $520 \text{ cm}^{-1}$  in the far-IR and changes are observed in the Si-O stretching mode region between  $1000$  and  $1300 \text{ cm}^{-1}$  in the mid-IR. This mode splitting is consistent with the doubling of the unit cell associated with the transition to the  $Pbn2_1$  phase observed using x-ray diffraction. It has been shown that the difference in wavenumber between the antisymmetric(asym.) and symmetric(sym.) stretching modes in silicates is a function of the intertetrahedral Si-O-Si bridging angle<sup>47</sup>. This difference decreases between the  $Cmc2_1$  and  $Pbn2_1$  phases (Table 4) due to a decrease in average intertetrahedral Si-O-Si bridging angle corresponding to the observed pore collapse.

The experimental results are in good agreement with the calculated infrared spectrum for the  $Pbn2_1$  phase (Figure 9). DFT calculations were also performed for the monoclinic  $P2_1$  structure. This structure was found to be dynamically unstable with two vibrational modes having negative frequencies. In addition, the agreement with the experimental IR spectrum was not as good as with the orthorhombic  $Pbn2_1$  structure. These results thus provide further evidence for the validity of the orthorhombic  $Pbn2_1$  structure for the high pressure phase of TON. DFT calculations also indicated that the initial empty pore  $Cmc2_1$  structure is also dynamically unstable with five vibrational modes having negative frequencies. This is consistent with the observation that the  $Cmc2_1$  to  $Pbn2_1$  transition and pore collapse is irreversible at least down to 0.3 GPa.

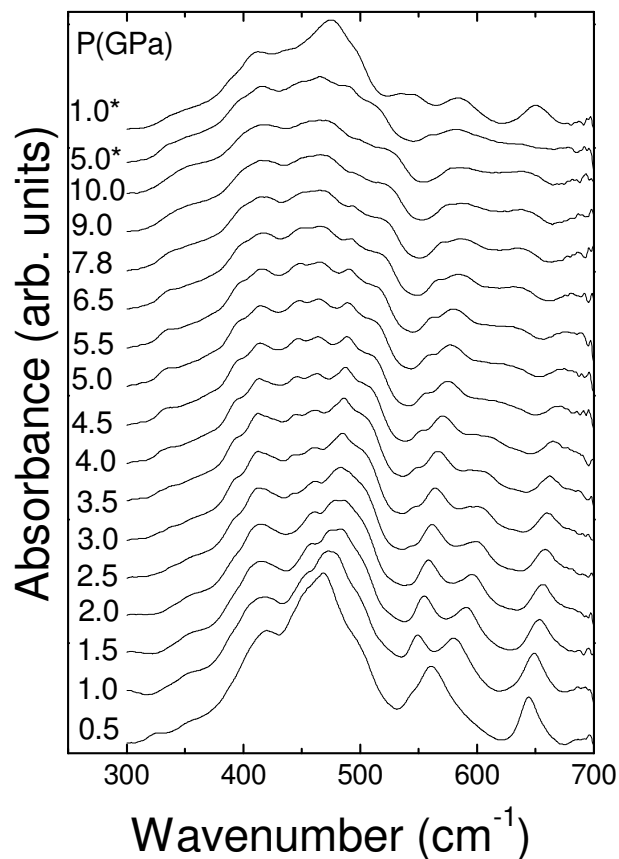


**Figure 7.** Far-infrared spectra of TON as a function of pressure. \* = data obtained on decompression from 10 GPa.

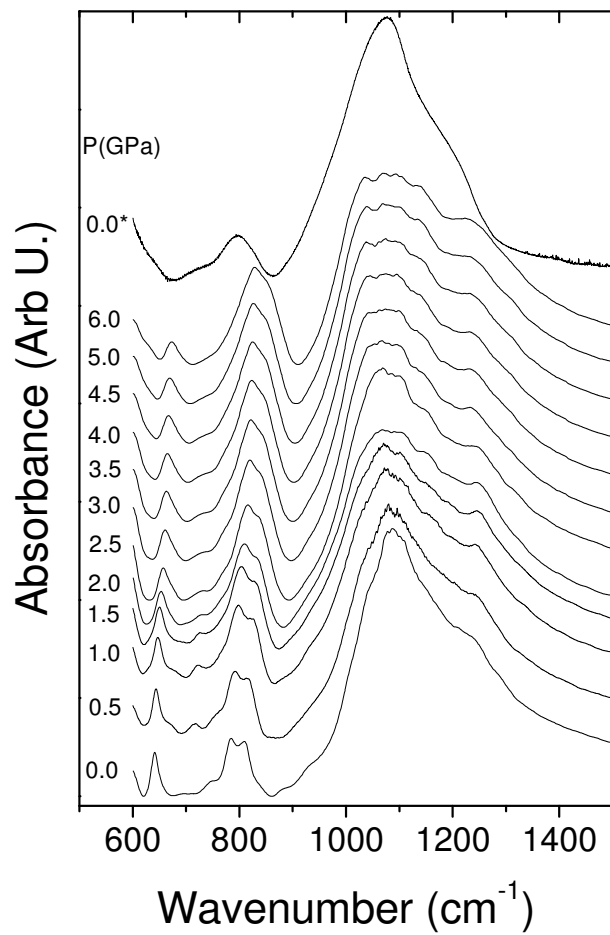


**Figure 8.** Mid-infrared spectra of TON as a function of pressure. \* = data obtained on pressure release from 15 GPa.

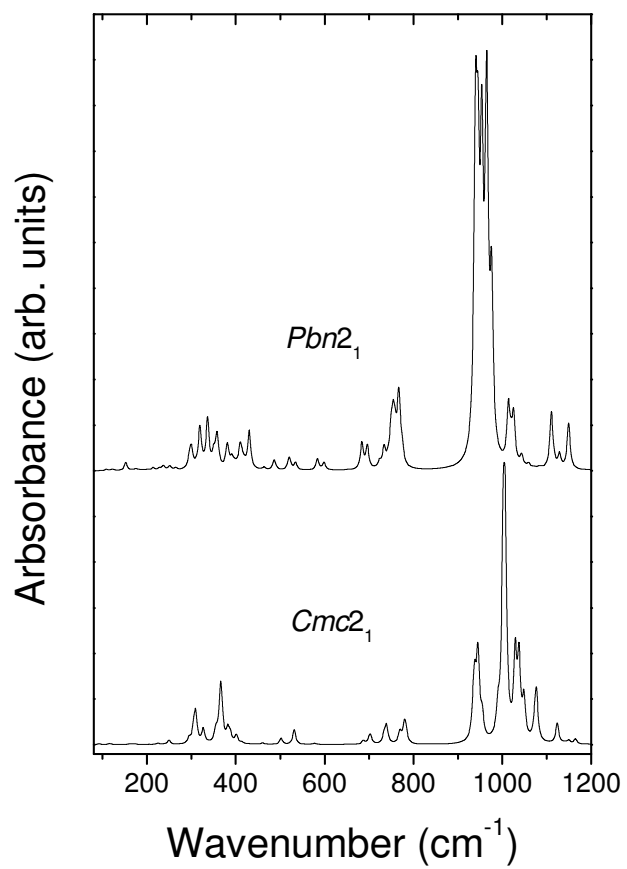


**Figure 9.** Calculated infrared spectra of the  $Cmc2_1$  structure of TON at ambient pressure (bottom) and the  $Pbn2_1$  structure at 2 GPa (top).



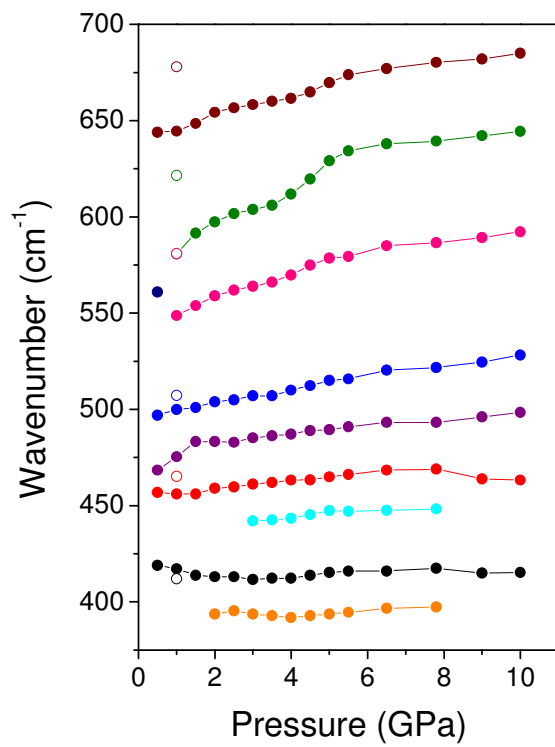
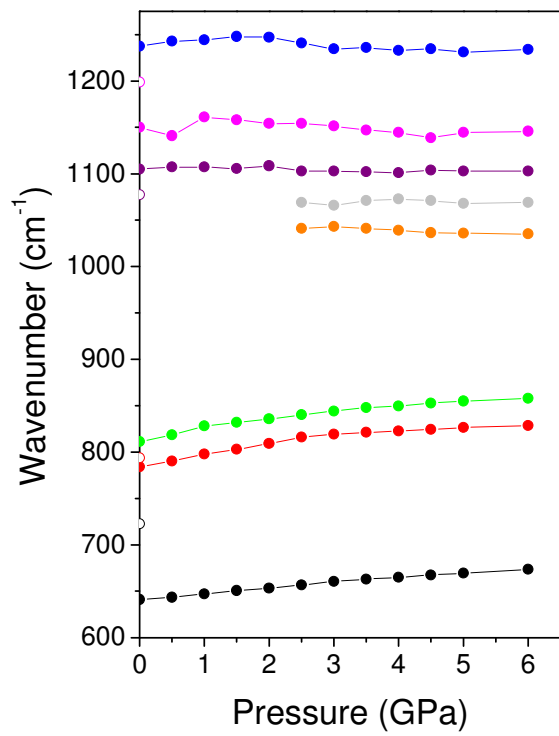


**Figure 10.** Pressure dependence of the mid(top)- and far(bottom)-infrared bands of TON. Open symbols correspond to data obtained on decompression.

**Table 4.** Selected infrared bands ( $\text{cm}^{-1}$ ) of the  $Cmc2_1$  structure of TON at 0.1 MPa and the  $Pbn2_1$  structure at 3 GPa and the amorphous form on decompression.

$Cmc2_1$ (0.5 GPa)	$Pbn2_1$ (3 GPa)	Amorphous (0.1 MPa/MIR, 1.0GPa/FIR)	Assignment <sup>45-46</sup>
1243	1235	1198	External asym. stretch
1141	1151		
1107	1103	1078	Internal asym. stretch
	1066		
	1043		
819	844		External sym. stretch
790	819	794	External sym. stretch
		722	
644	658	678	Internal asym. stretch
	604	622	
561	564	581	Secondary building unit ring vibration
497	507	507	
468	485	465	Si-O bending
457	461		Si-O bending
	442		
419	412	412	
	394		

Above 7 GPa, significant broadening of many modes was observed in the far-IR. This could be linked to progressive amorphization, in agreement with the x-ray diffraction results. It is only at this pressure that enough amorphous material has formed so that the broadening becomes evident. Upon decompression, the broad bands remain indicating that the amorphisation process is irreversible. There are some features in particular in the bending region, which are similar to those observed at low pressure indicating that the local structure consisting of rings of corner-sharing SiO<sub>4</sub> tetrahedra is retained. The observed wavenumbers of the modes observed on decompression are different to those observed on compression due to the important geometrical differences between the rings of tetrahedra in the collapsed amorphous form and the initial crystalline phase. The differences in wavenumber between the asymmetric and symmetric stretching modes for both internal and external tetrahedra are lower than in the crystalline *Cmc2<sub>1</sub>* and *Pbn2<sub>1</sub>* phases indicating lower average intertetrahedral Si-O-Si bridging angles corresponding to collapse pores.

#### **4. Conclusions**

The combined results of x-ray diffraction, infrared spectroscopy and DFT calculations have provided a detailed understanding of the high pressure phase transition and amorphization in the zeolite TON. Compression of the material involves two major steps. The first correspond to a

phase transition near 0.7 GPa from the  $Cmc2_1$  to a  $Pbn2_1$  structure involving a strong increase in the ellipticity of the pores, providing an additional compression mechanism involving changes in the intertetrahedral bridging angles in the  $SiO_2$  framework. The second step corresponds to irreversible, progressive pressure induced amorphization beginning above 4 GPa linked to pore collapse. The present results are useful to better understand the intrinsic high pressure behavior of TON and provide useful fundamental information on mechanical properties and phase stability of this material, which can be compared with filled-pore systems relevant for molecular spring applications and the preparation of nanocomposites.

#### ASSOCIATED CONTENT

**Supporting Information.** CIF files containing the structural data for the  $Cmc2_1$  and  $Pbn2_1$  structures have been supplied as supporting information. This material is available free of charge via the Internet at <http://pubs.acs.org>.

#### AUTHOR INFORMATION

##### **Corresponding Author**

\*Julien Haines

Julien.Haines@umontpellier.fr

##### **Author Contributions**

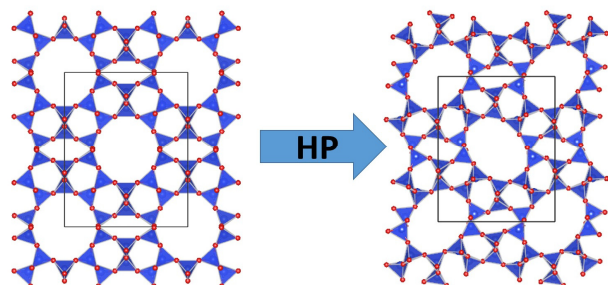
The manuscript was written through contributions of all authors. All authors have given approval to the final version of the manuscript.

## ACKNOWLEDGMENT

We are grateful for the support from PICS bilateral project CNR/CNRS (Italy/France), 2014-2016: Multifunctional zeolite/polymer nanocomposites. We acknowledge funding from the Agence Nationale de la Recherche program Investissements d'avenir in the framework of the contract ANR-10-LABX-05-01 (LabEx CheMISyst). We also thank the Deep Carbon Observatory (DCO) initiative under the project Physics and Chemistry of Carbon at Extreme Conditions and the Ente Cassa di Risparmio di Firenze under the project Firenze Hydrolab 2. K.D. acknowledges the Polish Ministry of Science and Higher Education for financial support through the "Mobilność Plus" program.

## REFERENCES

## Table of Contents Graphic



1. Gatta, G. D.; Nestola, F.; Ballaran, T. B., Elastic Behavior, Phase Transition, and Pressure Induced Structural Evolution of Analcime. *Am Mineral* **2006**, *91*, 568-578.
2. Haines, J.; Cambon, O.; Levelut, C.; Santoro, M.; Gorelli, F.; Garbarino, G., Deactivation of Pressure-Induced Amorphization in Silicalite SiO<sub>2</sub> by Insertion of Guest Species. *J Am Chem Soc* **2010**, *132*, 8860-8861.
3. Wells, S. A.; Sartbaeva, A.; Gatta, G. D., Flexibility Windows and Phase Transitions of Ordered and Disordered Ana Framework Zeolites. *Epl-Europhys Lett* **2011**, *94*, 56001.
4. Jorda, J. L., et al., Synthesis of a Novel Zeolite through a Pressure-Induced Reconstructive Phase Transition Process. *Angew Chem Int Edit* **2013**, *52*, 10458-10462.
5. Alabarse, F. G.; Brubach, J.-B.; Roy, P.; Haidoux, A.; Levelut, C.; Bantignies, J.-L.; Cambon, O.; Haines, J., Alpo4-54–Alpo4-8 Structural Phase Transition and Amorphization under High Pressure. *The Journal of Physical Chemistry C* **2015**, *119*, 7771-7779.
6. Gillet, P.; Malezieux, J. M.; Itie, J. P., Phase Changes and Amorphization of Zeolites at High Pressures: The Case of Scolecite and Mesolite. *Am Mineral* **1996**, *81*, 651-657.
7. Huang, Y. M., Ir Spectroscopic Study of the Effects of High Pressure on Zeolites Y, a and Sodalite. *J Mater Chem* **1998**, *8*, 1067-1071.
8. Huang, Y. N.; Havenga, E. A., Why Do Zeolites with Lta Structure Undergo Reversible Amorphization under Pressure? *Chem Phys Lett* **2001**, *345*, 65-71.
9. Liu, H. J.; Secco, R. A.; Huang, Y. N., Pressure-Induced Amorphization of Hydrated Na-X Zeolite. *Physchemcomm* **2001**, 1-3.
10. Rutter, M. D.; Uchida, T.; Secco, R. A.; Huang, Y.; Wang, Y., Investigation of Pressure-Induced Amorphization in Hydrated Zeolite Li-a and Na-a Using Synchrotron X-Ray Diffraction. *J Phys Chem Solids* **2001**, *62*, 599-606.
11. Comodi, P.; Gatta, G. D.; Zanazzi, P. F., High-Pressure Structural Behaviour of Heulandite. *Eur J Mineral* **2001**, *13*, 497-505.
12. Havenga, E. A.; Huang, Y. N.; Secco, R. A., An Investigation of the Effect of High Pressure on the Structure of Siliceous Zeolite Y. *Mater Res Bull* **2003**, *38*, 381-387.
13. Greaves, G. N.; Meneau, F.; Sapelkin, A.; Colyer, L. M.; Gwynn, I. A.; Wade, S.; Sankar, G., The Rheology of Collapsing Zeolites Amorphized by Temperature and Pressure. *Nat Mater* **2003**, *2*, 622-629.

14. Colligan, M.; Forster, P. M.; Cheetham, A. K.; Lee, Y.; Vogt, T.; Hriljac, J. A., Synchrotron X-Ray Powder Diffraction and Computational Investigation of Purely Siliceous Zeolite Y under Pressure. *J Am Chem Soc* **2004**, *126*, 12015-12022.
15. Greaves, N.; Meneau, F., Probing the Dynamics of Instability in Zeolitic Materials. *J Phys-Condens Mat* **2004**, *16*, S3459-S3472.
16. Greaves, G. N.; Meneau, F.; Kargl, F.; Ward, D.; Holliman, P.; Albergamo, F., Zeolite Collapse and Polyamorphism. *J Phys-Condens Mat* **2007**, *19*, 415102.
17. Isambert, A.; Angot, E.; Hebert, P.; Haines, J.; Levelut, C.; Le Parc, R.; Ohishi, Y.; Kohara, S.; Keen, D. A., Amorphization of Faujasite at High Pressure: An X-Ray Diffraction and Raman Spectroscopy Study. *J Mater Chem* **2008**, *18*, 5746-5752.
18. Haines, J.; Levelut, C.; Isambert, A.; Hébert, P.; Kohara, S.; Keen, D. A.; Hammouda, T.; Andrault, D., Topologically Ordered Amorphous Silica Obtained from the Collapsed Siliceous Zeolite, Silicalite-1-F: A Step toward “Perfect” Glasses. *J Am Chem Soc* **2009**, *131*, 12333-12338.
19. Readman, J. E.; Forster, P. M.; Chapman, K. W.; Chupas, P. J.; Parise, J. B.; Hriljac, J. A., Pair Distribution Function Analysis of Pressure Treated Zeolite Na-A. *Chemical Communications* **2009**, 3383-3385.
20. Hwang, G. C.; Shin, T. J.; Blom, D. A.; Vogt, T.; Lee, Y., Pressure-Induced Amorphization of Small Pore Zeolites-the Role of Cation-H<sub>2</sub>O Topology and Anti-Glass Formation. *Sci Rep-Uk* **2015**, *5*.
21. Vezzalini, G.; Arletti, R.; Quartieri, S., High-Pressure-Induced Structural Changes, Amorphization and Molecule Penetration in Mfi Microporous Materials: A Review. *Acta Crystallogr B* **2014**, *70*, 444-451.
22. Barri, S. A. I.; Smith, G. W.; White, D.; Young, D., Structure of Theta-1, the First Unidimensional Medium-Pore High-Silica Zeolite. *Nature* **1984**, *312*, 533-534.
23. Tzani, L.; Trzpit, M.; Souldard, M.; Patarin, J., High Pressure Water Intrusion Investigation of Pure Silica 1d Channel Afi, Mtw and Ton-Type Zeolites. *Micropor Mesopor Mat* **2011**, *146*, 119-126.
24. Santoro, M., et al., Synthesis of 1d Polymer/Zeolite Nanocomposites under High Pressure. *Chemistry of Materials* **2016**, *28*, 4065-4071.
25. Marler, B., Silica-Zsm-22: Synthesis and Single Crystal Structure Refinement. *Zeolites* **1987**, *7*, 393-397.
26. Papiz, M. Z.; Andrews, S. J.; Damas, A. M.; Harding, M. M.; Highcock, R. M., Structure of the Zeolite Theta-1. Redetermination Using Single-Crystal Synchrotron-Radiation Data. *Acta Crystallographica Section C* **1990**, *46*, 172-173.
27. Di Renzo, F.; Remoué, F.; Massiani, P.; Fajula, F.; Figueras, F.; Thierry Des, C., Crystallization Kinetics of Zeolite Ton. *Zeolites* **1991**, *11*, 539-548.
28. Murata, K., et al., Pressure Transmitting Medium Daphne 7474 Solidifying at 3.7 Gpa at Room Temperature. *Review of Scientific Instruments* **2008**, *79*, 085101.
29. Mao, H. K.; Xu, J.; Bell, P. M., Calibration of the Ruby Pressure Gauge to 800 Kbar under Quasi-Hydrostatic Conditions. *Journal of Geophysical Research: Solid Earth* **1986**, *91*, 4673-4676.
30. Hammersley, A. P.; Svensson, S. O.; Hanfland, M.; Fitch, A. N.; Hausermann, D., Two-Dimensional Detector Software: From Real Detector to Idealised Image or Two-Theta Scan. *High Pressure Res* **1996**, *14*, 235-248.

31. Rodriguez-Carvajal, J., Magnetic Structure Determination from Powder Diffraction Using the Program Fullprof. *Applied Crystallography* **2001**, 30-36.
32. Momma, K.; Izumi, F., Vesta 3 for Three-Dimensional Visualization of Crystal, Volumetric and Morphology Data. *J Appl Crystallogr* **2011**, *44*, 1272-1276.
33. Angel, R. J.; Gonzalez-Platas, J.; Alvaro, M., Eosfit7c and a Fortran Module (Library) for Equation of State Calculations. *Z Kristallogr* **2014**, *229*, 405-419.
34. Dalla Bernardina, S., et al., New Experimental Set-Ups for Studying Nanoconfined Water on the Ailes Beamline at Soleil. *Vib Spectrosc* **2014**, *75*, 154-161.
35. Sanchez-Portal, D.; Ordejon, P.; Artacho, E.; Soler, J. M., Density-Functional Method for Very Large Systems with Lcao Basis Sets. *Int J Quantum Chem* **1997**, *65*, 453-461.
36. Perdew, J. P.; Burke, K.; Ernzerhof, M., Generalized Gradient Approximation Made Simple. *Phys Rev Lett* **1996**, *77*, 3865-3868.
37. Grimme, S., Semiempirical Gga-Type Density Functional Constructed with a Long-Range Dispersion Correction. *J Comput Chem* **2006**, *27*, 1787-1799.
38. Hermet, P.; Bantignies, J. L.; Rahmani, A.; Sauvajol, J. L.; Johnson, M. R.; Serein, F., Far- and Mid-Infrared of Crystalline 2,2'-Bithiophene: Ab Initio Analysis and Comparison with Infrared Response. *J Phys Chem A* **2005**, *109*, 1684-1691.
39. King-Smith, R. D.; Vanderbilt, D., Theory of Polarization of Crystalline Solids. *Phys Rev B* **1993**, *47*, 1651-1654.
40. Parise, J. B.; Gier, T. E.; Corbin, D. R.; Abrams, L.; Jorgensen, J. D.; Prince, E., Flexibility of the Framework of Zeolite Rho. Structural Variation from 11 to 573 K. A Study Using Neutron Powder Diffraction Data. *The Journal of Physical Chemistry* **1984**, *88*, 2303-2307.
41. Jansen, E.; Schafer, W.; Will, G., R-Values in Analysis of Powder Diffraction Data Using Rietveld Refinement. *J Appl Crystallogr* **1994**, *27*, 492-496.
42. Toby, B. H., R Factors in Rietveld Analysis: How Good Is Good Enough? *Powder Diffraction* **21 (1)** **2006**.
43. Alabarse, F. G.; Rouquette, J.; Coasne, B.; Haidoux, A.; Paulmann, C.; Cambon, O.; Haines, J., Mechanism of H<sub>2</sub>O Insertion and Chemical Bond Formation in Alpo<sub>4-54</sub>Xh<sub>2</sub>o at High Pressure. *J Am Chem Soc* **2015**, *137*, 584-587.
44. Birch, F., Equation of State and Thermodynamic Parameters of Nacl to 300-Kbar in the High-Temperature Domain. *J Geophys Res-Solid* **1986**, *91*, 4949-4954.
45. Jacobs, P. A.; Martens, J., A. ; Eds., *Studies in Surface Science and Catalysis*; Elsevier, 1987; Vol. 33, p 3-44.
46. Bueno-Perez, R.; Calero, S.; Dubbeldam, D.; Ania, C. O.; Parra, J. B.; Zaderenko, A. P.; Merklng, P. J., Zeolite Force Fields and Experimental Siliceous Frameworks in a Comparative Infrared Study. *J Phys Chem C* **2012**, *116*, 25797-25805.
47. Lazarev, A. N., *Vibrational Spectra and Structure of Silicates*. Plenum Publishers: New York, 1972.